



Radiation hydrodynamic simulations of massive star formation via gravitationally trapped H II regions – spherically symmetric ionized accretion flows

K. Lund ¹★, K. Wood,¹ D. Falceta-Gonçalves,^{1,2} B. Vandenbroucke ¹, N. S. Sartorio,³ I. A. Bonnell,¹ K. G. Johnston⁴ and E. Keto⁵

¹*SUPA, School of Physics and Astronomy, University of St Andrews, North Haugh, St Andrews KY16 9SS, UK*

²*Escola de Artes, Ciências e Humanidades, Universidade de São Paulo, Rua Arlindo Bettio 1000, CEP 03828-000 São Paulo, Brazil*

³*Instituto Nacional de Pesquisas Espaciais – INPE, Divisão de Astrofísica, Av. dos Astronautas, 1.758 – Jardim da Granja, São José dos Campos – SP, Brazil*

⁴*School of Physics and Astronomy, E. C. Stoner Building, The University of Leeds, Leeds LS2 9JT, UK*

⁵*Harvard-Smithsonian Center for Astrophysics, 160 Garden Str, Cambridge, MA 02420, USA*

Accepted 2019 February 28. Received 2019 February 25; in original form 2018 November 16

ABSTRACT

This paper investigates the gravitational trapping of H II regions predicted by steady-state analysis using radiation hydrodynamical simulations. We present idealized spherically symmetric radiation hydrodynamical simulations of the early evolution of H II regions including the gravity of the central source. As with analytic steady-state solutions of spherically symmetric ionized Bondi accretion flows, we find gravitationally trapped H II regions with accretion through the ionization front on to the source. We found that, for a constant ionizing luminosity, fluctuations in the ionization front are unstable. This instability only occurs in this spherically symmetric accretion geometry. In the context of massive star formation, the ionizing luminosity increases with time as the source accretes mass. The maximum radius of the recurring H II region increases on the accretion time-scale until it reaches the sonic radius, where the infall velocity equals the sound speed of the ionized gas, after which it enters a pressure-driven expansion phase. This expansion prevents accretion of gas through the ionization front, the accretion rate on to the star decreases to zero, and it stops growing from accretion. Because of the time required for any significant change in stellar mass and luminosity through accretion our simulations keep both mass and luminosity constant and follow the evolution from trapped to expanding in a piecewise manner. Implications of this evolution of H II regions include a continuation of accretion of material on to forming stars for a period after the star starts to emit ionizing radiation, and an extension of the lifetime of ultracompact H II regions.

Key words: hydrodynamics – radiative transfer – stars: formation – stars: massive – H II regions.

1 INTRODUCTION

The classic picture of H II region evolution, as described in textbooks such as Spitzer (1978), envisages a source of ionizing radiation turning on in a uniformly dense medium and ignores the gravity of the source. The H II region initially grows with an ionization front expanding into neutral gas. This so-called rarefied or R-type phase happens rapidly and the gas structure is relatively unaffected. As the ionized gas is hotter than the neutral gas, the next stage sees the H II region grow by pressure-driven expansion, producing a double front structure where a shock front expands into neutral gas ahead of the

ionization front. At late times and large size scales, the assumption that gravity is neglected is valid and this model is very successful in explaining the dynamics and structures of old and large H II regions that are studied at optical and infrared wavelengths. However during early H II region evolution, the neglect of gravity presents a problem for the formation of massive stars because it assumes feedback from ionizing radiation will halt accretion as soon as the star turns on, thereby limiting the mass that can be attained.

In a series of papers, Keto (2002a,b, 2003) expanded on work presented by Mestel (1954) and examined the evolution of H II regions at size scales where the gravity of the central source dominates the gas dynamics. He first studied steady-state solutions for two-temperature spherically symmetric Bondi accretion (Bondi 1952), whereby a source of ionizing radiation creates a hot ($T_i \approx$

* E-mail: kblg@st-andrews.ac.uk

10^4 K) H II region within cold ($T_n \approx 100$ K) neutral inflowing gas. When the H II region is inside approximately the ionized sonic point, where the flow velocity equals the local sound speed, it is unable to expand and remains gravitationally trapped. Accretion occurs from the infalling cold neutral gas and continues inwards towards the star through the H II region boundary where the gas forms an ionized accretion flow. As the star accretes mass, its luminosity increases and the H II region grows in size, not due to pressure driven expansion, but because of the increasing ionizing luminosity. Eventually the H II region will grow to surpass the critical radius close to the sonic point, gravity of the central star will no longer dominate, and the H II region will begin a pressure-driven expansion. At this stage, accretion through the ionization front can no longer occur. Some of the already ionized gas will move outwards along with the expanding ionization front, but the innermost gas continues to accrete on to the star, and as the H II region is drained accretion halts. This marks the maximum mass the star can accrete in a spherically symmetric system and beyond this stage the H II region continues its pressure-driven expansion.

In subsequent papers (Keto & Wood 2006; Keto 2007), this work was extended to consider H II region evolution within rotationally flattened structures. In this two-dimensional picture, the H II region grows more rapidly into the lower density regions, creating a bipolar outflow. Accretion of ionized material continues through the dense mid-plane until the ionizing luminosity increases the size of the H II region beyond the critical radius for gravitational trapping in the mid-plane, thereby shutting off accretion similar to the spherical case. In some scenarios, however, the mid-plane regions are so dense that they are shielded from radiation. Consequently, accretion on to the star through these regions would not be halted by ionization feedback, but by some other process (Nakano 1989; Yorke & Sonnhalter 2002; Krumholz et al. 2009; Kuiper et al. 2010; Harries, Douglas & Ali 2017; Kuiper & Hosokawa 2018).

This picture of massive star formation through gravitationally trapped H II regions is appealing in that it overcomes the mass limits set by ionization feedback in the classic picture where gravity is ignored. It also means that the time-scale for the growth of the H II region initially depends on the accretion time-scale and is not solely due to the rate of the pressure-driven expansion. This provides a potential solution to the lifetime problem for ultracompact (UC) H II regions; the number of UCH II regions found in the Wood & Churchwell (1989) survey suggests they have a longer lifetime than predicted by pressure-driven expansion of an UCH II region into a diffuse H II region.

This theoretical framework can also explain observations of massive star-forming regions that show infall velocities in molecular gas at large-size scales that smoothly match on to infall velocities in ionized gas at smaller size scales (Keto 2002a; Sollins et al. 2005a). Observations showing both inflow and outflow (Sollins et al. 2005b; Klaassen & Wilson 2007; Klaassen et al. 2018) are explained with the picture of H II region evolution in axisymmetric rotationally flattened structures.

The analysis presented by Keto (2002b, 2003) and Mestel (1954) modelled the H II region evolution as a sequence of steady-state solutions with increasing ionizing luminosity. We extend this work by running simulations of the same process to provide a consistent radiation hydrodynamic evolution. In this paper, we present numerical simulations from our radiation hydrodynamic code of spherically symmetric ionized accretion flows. Our code reproduces the main features described in the works of Mestel and Keto. We find that gravitationally trapped H II regions naturally

arise within the ionized sonic point, but are unstable in spherical geometries.

Future papers will study the spherically symmetric instability in more detail and move on to two-dimensional axisymmetric and three-dimensional simulations. Section 2 describes our radiation hydrodynamic code, Section 3 presents results for spherical ionized accretion flows, and we present our conclusions in Section 4.

2 RADIATION HYDRODYNAMIC CODE

Our code is described in detail in an upcoming paper, but the main features are briefly outlined here. In order to simulate the plasma dynamics as it is impacted by the effect of ionization, we have coupled a magnetohydrodynamical (MHD) code, modified from a publicly available GODUNOV code¹ (Kowal, Falceta-Gonçalves & Lazarian 2011; Falceta-Gonçalves et al. 2015; Falceta-Gonçalves & Kowal 2015; Kowal et al. 2017; Santos-Lima et al. 2017), with a time-independent Monte Carlo radiation transfer (MCRT) code for photoionization. Even though the code is able to deal with magnetic fields, for the purposes of this work, these have been neglected. Real collapsing cores in the interstellar medium are indeed magnetized; however, the main goal of this work is the direct comparison of our numerical models to an unmagnetized analytical framework. Also, not only are full radiative MHD models computationally expensive compared to an HD approximation, MHD waves would be allowed to grow, propagate and non-linearly interact with other perturbations of the fluid. This would make the comparison to the analytical model irrelevant.

The code evolves compressible fluid dynamics in a 3D Cartesian grid by solving the set of hydrodynamical equations, solved in the conservative form as

$$\partial_t U + \nabla \cdot \mathbf{F}(U) = f(U), \quad (1)$$

where U is the vector of conserved variables:

$$U = \left[\rho, \rho \mathbf{v}, \left(\frac{1}{\gamma - 1} p + \frac{1}{2} \rho v^2 \right) \right]^T, \quad (2)$$

F is the flux tensor:

$$F = \left[\rho \mathbf{v}, \rho \mathbf{v} \mathbf{v} + p \mathbf{I}, \left(\frac{\gamma}{\gamma - 1} p + \frac{1}{2} \rho v^2 \right) \mathbf{v} \right]^T, \quad (3)$$

and f corresponds to source terms for the given conserved variable U . ρ represents the gas mass density, \mathbf{I} is the identity matrix, \mathbf{v} is the fluid velocity, p is the thermal pressure, and γ is the adiabatic polytropic index. We use the equation of state $p \propto \rho^\gamma$ with $\gamma = 1.001$ to mimic an isothermal equation of state, as the cooling time in the scenario we are considering is much shorter than the hydrodynamical time-scale.

The spatial reconstruction is obtained by means of a third-order monotonicity-preserving method (He et al. 2011), with flux piecewise discontinuity being solved approximately by the HLLC Riemann solver (Mignone & Bodo 2006). The time evolution is done by means of the third-order four-stage explicit Strong Stability Preserving Runge–Kutta method (Ruuth 2006), with a Courant–Friedrichs–Lewy (CFL) of 0.2.

In the GODUNOV scheme, the hydrodynamical equations are first solved in conserved form, and any external source term (e.g. gravity) is calculated as an update to the physical conserved

¹<https://bitbucket.org/amunteam/godunov-code>

variables (mass, momentum, and energy) afterwards. The gravity term has been included as a point source mass at the grid centre. For the sake of simplicity, the gravitational effect of the interstellar gas on the central source is not being considered in this work, therefore the point source is assumed to be fixed. Photoionization is also treated in our numerical scheme as a source term for the energy equation, being obtained from the MCRT module. The energy density transferred to the gas as a MC photon packet is absorbed is $\delta\epsilon \simeq 2 \times \frac{3}{2}nk(T_{\text{MC}} - T_{\text{n}})$, where n is the number density, k is the Boltzmann constant, T_{MC} represents the temperature of equilibrium of the ionized gas (see equation 8), and T_{n} represents the neutral gas temperature. The factor of 2 multiplying the thermal energy difference corresponds to the assumption that ionization generates ions and electrons in a number twice that of neutral gas.

The principle of MCRT is modelling photon propagation using probability distributions. For the specific workings of the Monte Carlo photoionization code we are using, see Wood & Reynolds (1999), Wood & Loeb (2000), and Wood, Mathis & Ercolano (2004). For each time-step of the hydrodynamical code, the 3D density grid is exported to the MCRT module. The MCRT module is therefore considered time-independent, and equilibrium reached quasi-instantaneously compared to the dynamical time-scale of the system. This assumption is adequate given that the typical radiative time-scales, namely the light crossing-time $\tau_{\text{light}} \sim Lc^{-1}$ and the recombination time $\tau_{\text{recomb}} \sim (n_e \alpha_A)^{-1}$, are much shorter than the hydrodynamical time-scale $\Delta t \sim L \max(u)^{-1}$.²

For simplicity, the material in the grid is assumed to be 100 per cent hydrogen, with no heavier elements and no dust. Our aim is to determine the ionization structure of hydrogen, and assuming pure hydrogen is sufficient for that purpose. Including heavy elements is important for cooling rates, but their low abundances and hence small opacities relative to hydrogen do not influence the radiation transport and the resulting ionization structure of hydrogen (Wood et al. 2004). We let the fixed gravitational point source at the centre of the grid also be an ionizing point source with a specific luminosity. This ionizing source emits packets of photons isotropically, which are tracked through a random walk of photoionizations and photon re-emissions until the packet either escapes the grid or is re-emitted as non-ionizing photons. We are assuming instantaneous photoionization equilibrium, so there is no time dependence. We do not consider a full spectrum for the photon frequencies, but apply a two-frequency approximation for the MCRT photoionization code (see detailed description and benchmark tests in Wood & Loeb 2000). Stellar photons, those originating from the source, are given an energy of 17.9 eV, representing an average frequency for ionizing photons originating from a 40 000 K star (see the appendix of Wood & Loeb 2000). Diffuse photons, meaning the re-emitted ionizing photons, are given an energy of 13.6 eV, as they have a spectrum which is strongly peaked around that value. We record the distances travelled by each photon packet within the grid cells they pass through, along with whether that distance was travelled by stellar or diffuse photons.

After tracking all photon packets we balance the number of photoionizations and recombinations per unit of time to obtain the ionization fraction in each grid cell:

$$n_{\text{H}^0} \int_{\nu_0}^{\infty} \frac{4\pi J_{\nu}}{h\nu} \sigma_{\nu} d\nu = \alpha_A n_e n_p. \quad (4)$$

²Here, L represents the scale of the system, c is the speed of light, n_e is the electron density, α_A the recombination coefficient to all levels, and $\max(u)$ is the maximum local speed detected over all cells of the simulated cube.

α_A is the recombination coefficient to all levels (e.g. $\alpha_A \approx 5.25 \times 10^{-13} \text{ cm}^3 \text{ s}^{-1}$ for hydrogen at $T = 8000 \text{ K}$, based on table 2.1 in Osterbrock & Ferland 2006), h is the Planck constant, J_{ν} is the mean intensity at frequency ν , and $h\nu_0 = 13.6 \text{ eV}$. n_{H^0} is the number density of neutral hydrogen, n_e is the number density of electrons, and n_p is the number density of protons that we can rewrite as the number density of ionized hydrogen, n_{H^+} . Assuming pure hydrogen in ionization equilibrium the number of electrons equals the number of protons, hence $n_p n_e = n_{\text{H}^+}^2$. Using path-length estimators in the MCRT code (Lucy 1999), the integral can be rewritten for each cell as

$$I = \int_{\nu_0}^{\infty} \frac{4\pi J_{\nu}}{h\nu} \sigma_{\nu} d\nu = \frac{Q}{NV} \sum l\sigma_{\nu}, \quad (5)$$

where Q is the ionizing luminosity, N is the number of photon packets, and V is the volume of the cell. From our tracking of the photon packets, we can calculate $\sum l\sigma_{\nu}$; the sum of all the path-lengths travelled through that specific grid cell times the cross-section corresponding to the type of photons (stellar or diffuse) responsible for each path-length. By splitting the total number density of hydrogen into a neutral and an ionized component:

$$n_{\text{H}} = n_{\text{H}^0} + n_{\text{H}^+}, \quad (6)$$

the equilibrium equation can be rewritten as a quadratic equation:

$$\alpha_A n_{\text{H}^+}^2 + \text{In}_{\text{H}^+} - \text{In}_{\text{H}} = 0. \quad (7)$$

At the end of each MCRT iteration, we solve equation (7) in each cell to get the neutral gas fraction, $n_{\text{frac}} = n_{\text{H}^0}/n_{\text{H}}$. The ionization fraction, and hence opacity, of each cell is updated to their new values. The code runs through 10 iterations before we accept the current ionization structure and opacity values.

In order to get reliable results, the code needs to run through a substantial number of photon packets; we use 100 000 packets for the first 7 iterations and 10 times more for the last 3. Considering the photon density will decrease at larger distances from the source, the larger the simulation box size, the more photon packets are needed to get good statistics for the Monte Carlo estimators for the ionization rate in the outer parts, similar to ray tracing techniques. Since we are studying spherically symmetric accretion, we have introduced a radial averaging scheme that uses symmetry to get better signal-to-noise ratio without having to increase the number of photon packets. This results in spherically symmetric idealized 3D MCRT simulations. We observe that increasing the number of photon packets by a factor of 10 does not change the calculated ionization structure noticeably, but increases the computational time. Consequently, we assume 10 iterations using our original number of photon packets combined with the radial averaging scheme is sufficient.

In reality, there are a number of heating and cooling processes governing the temperature of the gas, but the net result is a temperature of approximately 8000 K for photoionized solar metallicity gas, see for example Wood et al. (2004). Although we only need to consider hydrogen opacity to determine the ionization structure, setting the temperature of ionized gas to be 8000 K approximates the existence of other elements that provide cooling to give this temperature for photoionized gas. By assigning fixed temperatures for neutral and ionized gas, T_{n} and T_{i} , respectively, we can determine the temperature for any given ionization fraction using the common approximation (Haworth & Harries 2012)

$$T_{\text{MC}} = T_{\text{n}} + (T_{\text{i}} - T_{\text{n}})(1 - n_{\text{frac}}). \quad (8)$$

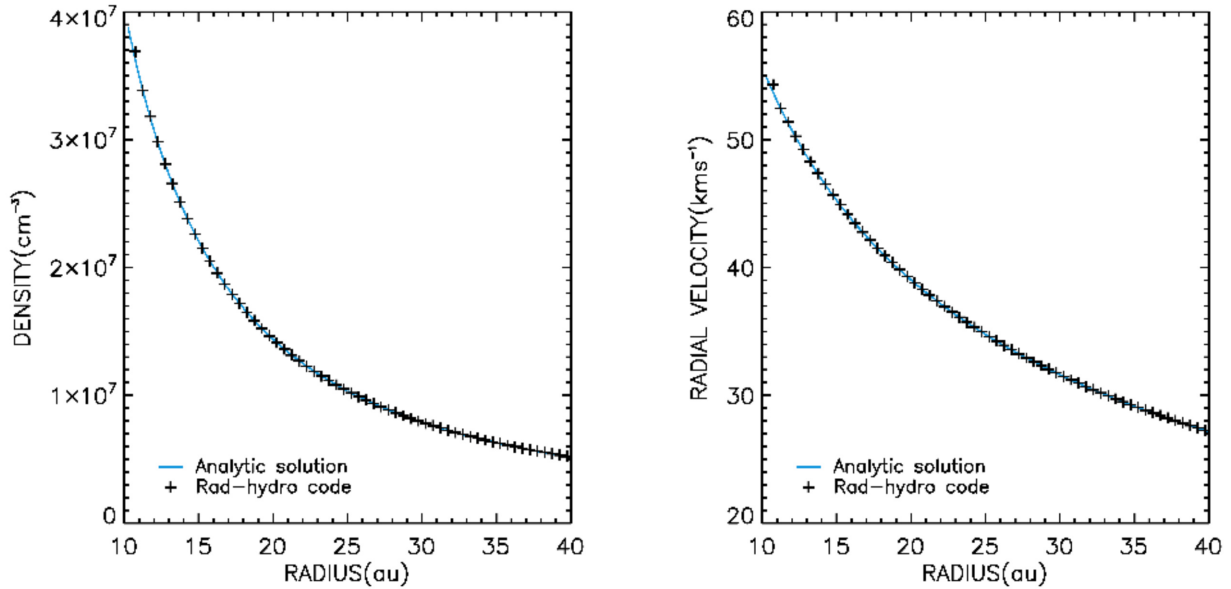


Figure 1. Radially averaged steady-state density (*left*) and inflow velocity (*right*) from the rad-hydro simulation of material accreting on to a central source compared to the analytic Bondi accretion solution (Vandenbroucke et al. 2019).

Once the ionized and neutral gas temperatures are given by the MCRT module, the pressure tensor in the hydrodynamic code is updated.

The code described above has already been successfully tested and benchmarked for the standard Spitzer solution of spherical expansion of an H II region in a uniform medium (Falceta-Gonçalves, in preparation). This benchmark test (Bisbas et al. 2015) shows our code reproduces the slow D-type expansion of an H II region. In Section 3.3, we show that when the ionization radius is held fixed our code also reproduces the analytic steady-state solution for a fast two temperature R-type accretion flow.

Throughout our paper, we adopt the usual definitions for D-type and R-type ionization fronts (Osterbrock & Ferland 2006) where the relative velocity, v_r , between the ionization front and neutral gas is defined by two critical conditions:

$$v_r \leq c_i - \sqrt{c_i^2 - c_n^2} = v_D \approx \frac{c_n^2}{2c_i} \quad (9)$$

and

$$v_r \geq c_i + \sqrt{c_i^2 - c_n^2} = v_R \approx 2c_i, \quad (10)$$

where c_i and c_n are the sound speeds in the ionized and neutral gas. Velocities lower than v_D result in a subsonic D-type front, and velocities higher than v_R results in a supersonic R-type front.

3 RAD-HYDRO SIMULATIONS OF SPHERICAL IONIZED ACCRETION FLOWS

The purpose of this paper is to investigate the gravitational trapping of H II regions predicted by steady-state analysis using radiation hydrodynamical simulations. Starting with a central star where gravity causes a spherically symmetric accretion flow we are interested in the gas dynamics when we turn on radiation at size scales where the infall velocities of the accreting gas exceed the R-critical condition (equation 10).

We use a non-adaptive Cartesian grid to simulate our region of interest, we are not concerned with what happens to the gas outside

our simulation box, nor the details of how material gets on to the central star. In the following simulations, we will not update the mass and luminosity of the star during accretion. We are dealing with an accretion rate of $\sim 4 \times 10^{-7} M_\odot \text{yr}^{-1}$, which implies a time-scale of megayears to accrete $1 M_\odot$ of material on to the star. Considering our simulations run over tens to hundreds of years, any significant change in mass and luminosity will occur over time-scales much greater than those investigated here.

3.1 Steady-state Bondi accretion

We include the gravity of a central star in the code by adding source terms to the momentum and energy hydrodynamical equations. When we consider the gravitational pull of the central star to be the only force acting the result is known as Bondi accretion: spherically symmetric inflow with a constant accretion rate (Bondi 1952). Before switching on radiation, we want to make sure our code can reproduce the behaviour associated with Bondi accretion. We compare the results from our simulations with analytical expressions for the expected density and velocity as a function of radius, shown as the blue lines in Fig. 1. For a derivation of these expressions from the constant Bondi accretion rate, see Vandenbroucke et al. (2019).

Due to the gravitational force, there will be a progressively steeper increase in density and velocity closer to the source, with a singularity at the origin. We resign ourselves to not being able to resolve the physics close to the source and encase the region in a mask, inside which we specify a sink of constant density and in general no change of any variables as the simulation runs. Effectively any material that would have accreted on to the star disappears once it passes through the mask.

As an outer boundary condition, we set an external sphere with constant physical properties. The outer mask is a way of effectively transforming the cubed computational domain into a sphere, with less spurious numerical fluctuations. In every simulation presented in this paper, the region outside the sphere is set to follow the analytic Bondi accretion profile and provides a constant inflow of

Table 1. Basic simulation properties. Columns show, respectively, stellar mass, density at the neutral Bondi radius, neutral gas temperature, ionized gas temperature, radius of inner mask, radius of outer mask, and number of grid cells in each direction.

M_* (M_\odot)	ρ_B (cm^{-3})	T_n (K)	T_i (K)	Inner mask (au)	Outer mask (au)	Grid cells
17.87	30 000	500	8000	10.4	38.0	128

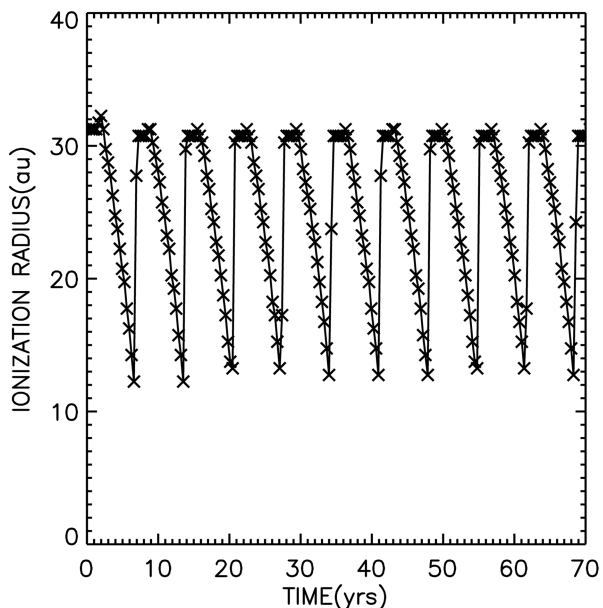


Figure 2. Ionization front radius as a function of time during the simulation of an $17.87 M_\odot$ central star with constant ionizing luminosity. Zero year marks the moment radiation is switched on.

material, consistent with the pull from the central mass. To set up the initial accretion, we define the central mass of the star, M_* , the neutral sound speed, c_n , and the density at the neutral Bondi radius,³ ρ_B .

When picking the initial parameters of the simulation, we want to ensure physically plausible values within a size scale where we can observe radial velocities exceeding the R-critical value; in this paper, we define a positive radial velocity as pointing towards the central source. We use the term R-critical radius for the position where the infall velocity equals the R-critical velocity. At the centre of the grid, we place an $17.87 M_\odot$ star. The simulation region must be closed enough to this star that the infall velocity will be high enough to observe R-type behaviour once we turn on ionization. We simulate $x, y, z \in [-40, 40]$ au, each direction being divided into 128 cells. The inner and outer masks have radii of 10.4 and 38.0 au, respectively. The density at the neutral Bondi radius is $30\,000 \text{ cm}^{-3}$, and all the gas is neutral with a temperature of 500 K,⁴ which corresponds to a sound speed of $\sim 2.0 \text{ km s}^{-1}$. Once the gas is fully ionized, the temperature increases to 8000 K, and the sound speed is approximately 11.5 km s^{-1} , which results in an R-critical

³The neutral Bondi radius is where the infall velocity equals the neutral sound speed.

⁴The choice of a somewhat high temperature is because the numerical simulations runtime scales upward as the temperature difference between ionized and neutral parts increases, and we wanted the simulations to be concluded in the computational time available.

velocity of $v_R \approx 23.0 \text{ km s}^{-1}$. The parameters are summarized in Table 1 and are also used for the simulations in Sections 3.2 and 3.3.

For the initial set-up of the Bondi accretion simulation, every parameter in the region of interest between the inner and outer masks is kept constant, the density is left as the value at the outer mask boundary, and the velocity is zero. The system is then allowed to evolve in time, with the gravity of the central star being the only external force source present. The code reached a steady state which, in Fig. 1, is shown to match the Bondi profiles. The densities and velocities plotted are obtained by radially averaging throughout the simulation box. The entire simulation region has infall velocities above v_R , which is the condition placed upon our chosen initial parameters. Note the steady-state Bondi profile, which we have been able to reproduce here, will be the starting point for all subsequent simulations.

3.2 Accretion on to a source with constant ionizing luminosity

Starting from the stable Bondi accretion structure described in the previous section, we turn on radiation of a fixed luminosity from the central star. We pick an ionizing luminosity of $Q = 2.5 \times 10^{46} \text{ s}^{-1}$, chosen such that the star initially ionizes material out to a radius of ~ 32 au. Notice that, because of the use of an internal mask, the value of Q in the simulations corresponds to the remaining ionizing photon luminosity at the mask radius, and not the stellar luminosity itself. Considering the complete ionization of the gas within the inner mask, we find Q corresponds to ~ 3 per cent of the central source ionizing luminosity, in agreement with a $\sim 18 M_\odot$ star (Vacca, Garmany & Shull 1996).

Based on knowing the ionization fraction in each grid cell, the ionization radius is determined by radially averaging the neutral gas fractions, using bins spanning approximately half a cell width, then looping through these bins in radial order until the neutral fraction equals or exceeds 0.5. The centre of the corresponding bin is defined to be the ionization radius. Fig. 2 shows this radius of the ionized region as a function of time. When we turn on the radiation the star ionizes a region out to ~ 32 au, but then the ionization front proceeds to shrink until it disappears within the inner mask and then moves back out. This process recurs on a 7 yr time-scale.

Fig. 3 shows four snapshots of the density and velocity profile of the system at different times during the first collapse of the H II region. The different colours correspond to different times and the vertical lines mark the ionization radius. There is a growing density peak around the ionization radius that moves inwards as the H II region shrinks. We can explain the appearance of an initial density perturbation by considering the jump conditions across the ionization front. Assuming $v_n \geq v_R \gg c_n$, it can be shown that (Osterbrock & Ferland 2006)

$$\frac{\rho_i}{\rho_n} \approx 1 + \frac{c_i^2}{v_n^2}. \quad (11)$$

Consequently, there will be a density increase in the ionized gas, and a corresponding decrease in velocity.

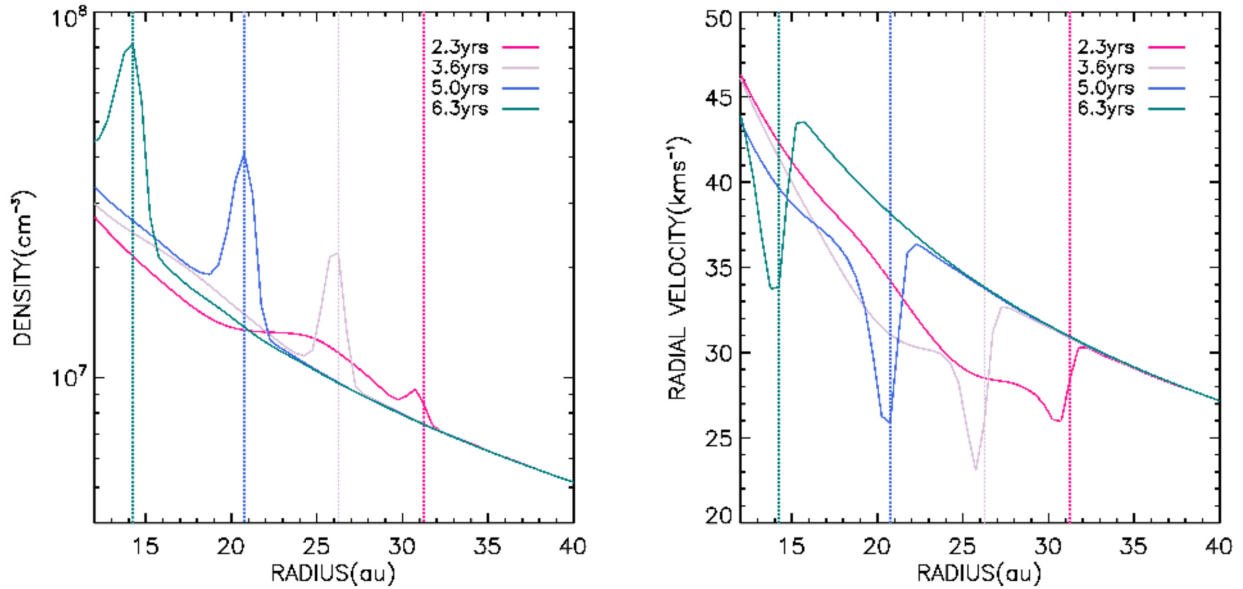


Figure 3. Radially averaged density (*left*) and inflow velocity (*right*) at four different times during the simulation of an $17.87 M_{\odot}$ central star with constant ionizing luminosity. The vertical lines represent the position of the ionization front. Zero year marks the moment radiation is switched on.

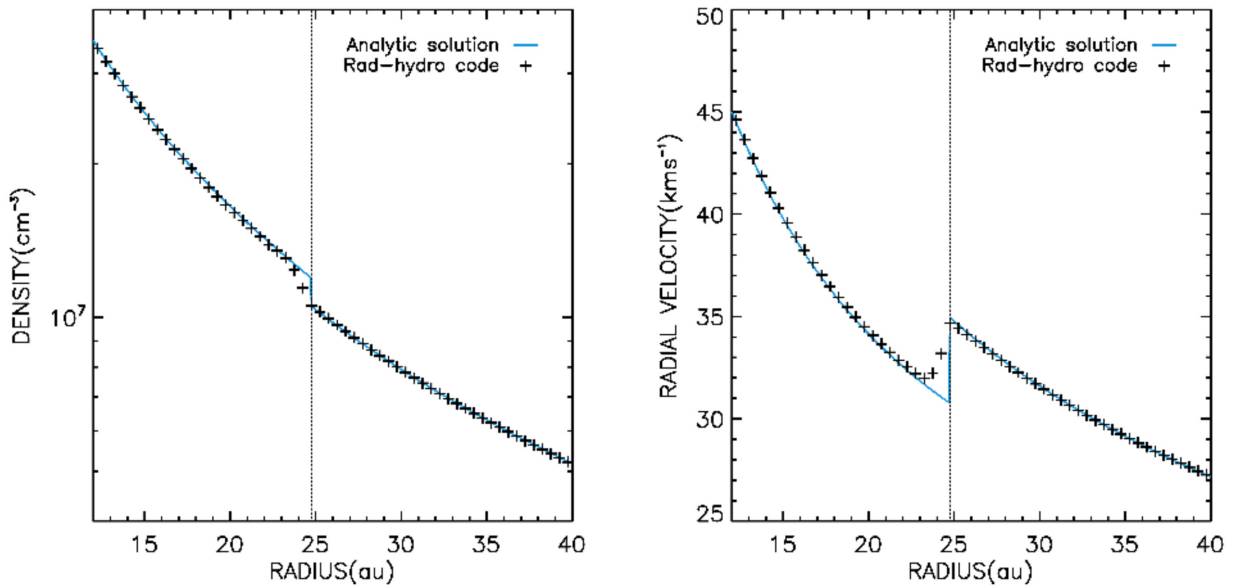


Figure 4. Radially averaged steady-state two-temperature density (*left*) and inflow velocity (*right*) from our rad-hydro simulation compared to the analytic solution (Vandenbroucke et al. 2019). The simulation forces an H II region out to the fixed radius $R_i = 24.75$ au, the vertical line represents the position of the ionization front.

The increase in density leads to an increased recombination rate, so the fixed ionizing luminosity cannot ionize to the same radius at the next time-step of the radiation hydrodynamic simulation. Material keeps piling up at the front and the density increases because the inflow velocity of material is greater outside the ionized region than inside. As the density peak grows the ionization radius must shrink further, resulting in the runaway behaviour shown in Fig. 3.

When the ionization front and the density enhancement reaches the inner mask, we assume it accretes on to the central star. As the density peak disappears inside the mask the amount of material inside the ionized region decreases drastically and in response the ionization front expands. The region outside the ionization front

has returned to a neutral Bondi profile, meaning the problem is essentially reset and the process repeats. For the parameters of this simulation, the H II region oscillates from just outside the inner mask to a maximum radius $R_{\max} \approx 31$ au over a regular period of ~ 7 yr.

Peters et al. (2010) also found flickering in their H II simulations. Whilst we are considering spherically symmetric accretion on to a single star, Peters et al. (2010) ran a 3D simulation on a much larger size scale (several parsec) of the collapse of a rotating molecular cloud. In our case, the contraction of the H II region is triggered by jump conditions at the R-type ionization front leading to a density peak, in contrast Peters et al. (2010) flickering was due to large-scale variations in the accretion flow.

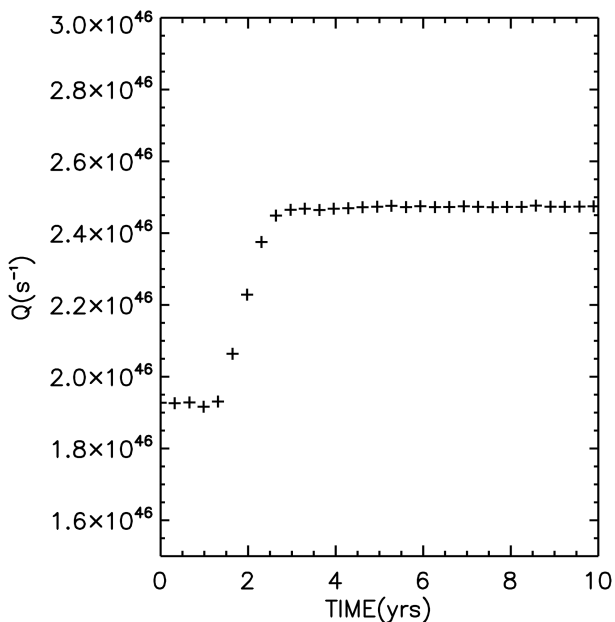


Figure 5. Ionizing luminosity, Q_{R_i} , required to maintain an H II region out to the fixed radius $R_i = 24.75$ au as a function of time. Zero year marks the moment radiation is switched on.

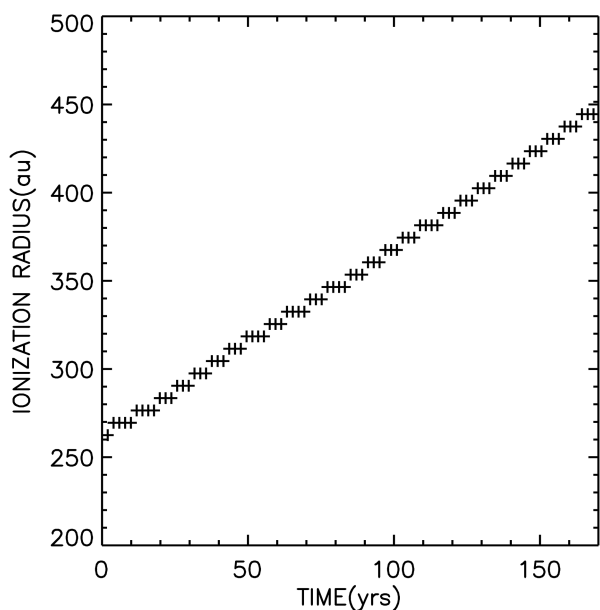


Figure 6. Ionization front radius as a function of time during the late-time simulation of an $17.87 M_{\odot}$ central star with constant ionizing luminosity. Time zero year marks the moment radiation is switched on.

According to Mestel (1954) and Keto (2002b, 2003), if the initial H II region starts out close enough to the star to be in the R-type regime it should be possible to prevent expansion, and keep accretion going with material moving through the ionized region. Our simulation of this scenario continuously accretes material on to the star and successfully traps the H II region within a radius R_{\max} , but it is not a steady-state solution as we observe recurring expansion and contraction.

Further investigation into the properties of this instability is being carried out analytically, with a 3D code, and a 1D code capable of

much higher time and spatial resolution, see Vandenbroucke et al. (2019). They find the 7 yr time-scale observed roughly corresponds to the local free-fall time at the ionization front radius, as the instability is caused by a small increase in density that is accreted on to the central mask within this time-scale and then reseeded. Furthermore, the recurring expansion and contraction of the H II region seems to be a result of the idealized spherically symmetric geometry caused by the radial averaging of the photoionization in fully 3D simulations the same behaviour is not observed.

3.3 Steady-state two-temperature accretion

In the previous section, we showed our code produced a gravitationally trapped, but oscillating, H II region. Next, we aim to produce a steady-state two-temperature accretion solution by forcing the ionization radius to remain constant in time.

Again we start from a stable neutral Bondi accretion flow, but instead of switching on a constant ionizing luminosity, Q , we set the ionizing luminosity, Q_{R_i} , before each call to the radiation transfer scheme to be the value that will fully ionize gas out to a prescribed radius, $R_i = 24.75$ au. This is determined by balancing photoionization with radiative recombination (adopting on-the-spot approximation) inside the radius R_i :

$$Q_{R_i} = \Sigma n^2 \alpha_B \Delta V, \quad (12)$$

where the sum is over all cells with a radius $r \leq R_i$, n is the number density, $\alpha_B = 2.5 \times 10^{-13} \text{ cm}^3 \text{ s}^{-1}$ is the Case B recombination coefficient for hydrogen at 8000 K, and ΔV is the volume of a cell.

The size of the ionized region is kept constant, and as a consequence, instead of a high-density peak at the ionization front, after ~ 3 yr the entire ionized region settles to a stable higher density profile. Fig. 4 shows the final accretion profile follows closely the analytic solution for steady-state two-temperature Bondi accretion (Vandenbroucke et al. 2019). As this higher density region builds up, the luminosity required to ionize it will have to increase until the steady-state two-temperature accretion structure is reached. Fig. 5 shows that the ionizing luminosity required to maintain this structure increases in time to an almost constant value. If we stop calculating the luminosity, but keep it constant once the steady-state solution is reached, in time the simulation returns to the oscillatory behaviour described in Section 3.2 due to numerical noise in the rad-hydro code.

In conclusion, we only reach a steady-state two-temperature accretion solution with careful fine-tuning of the ionizing luminosity, and once the solution is reached it is not stable, evolving into a runaway instability to any fluctuation (including numerical noise).

3.4 Late-time evolution

As material accretes on to stars and they grow in mass, we expect their luminosity to grow correspondingly, meaning they can ionize increasingly larger volumes. As previously mentioned, this increase in mass and luminosity happens over greater time-scales than those we are considering; hence, we simulate the evolution of the ionized region piecewise, keeping the mass and luminosity constant during each stage. We have so far only considered H II regions close enough to the star for the infall velocity to exceed v_R , where the ionization front exhibits an R-type behaviour. In this phase, we have found that the H II region is gravitationally trapped and oscillating. Once the relative velocity of the ionization front decreases below v_D , it will transition to D-type. At this point, gravity is no longer dominant and the ionization front experiences a pressure-driven expansion.

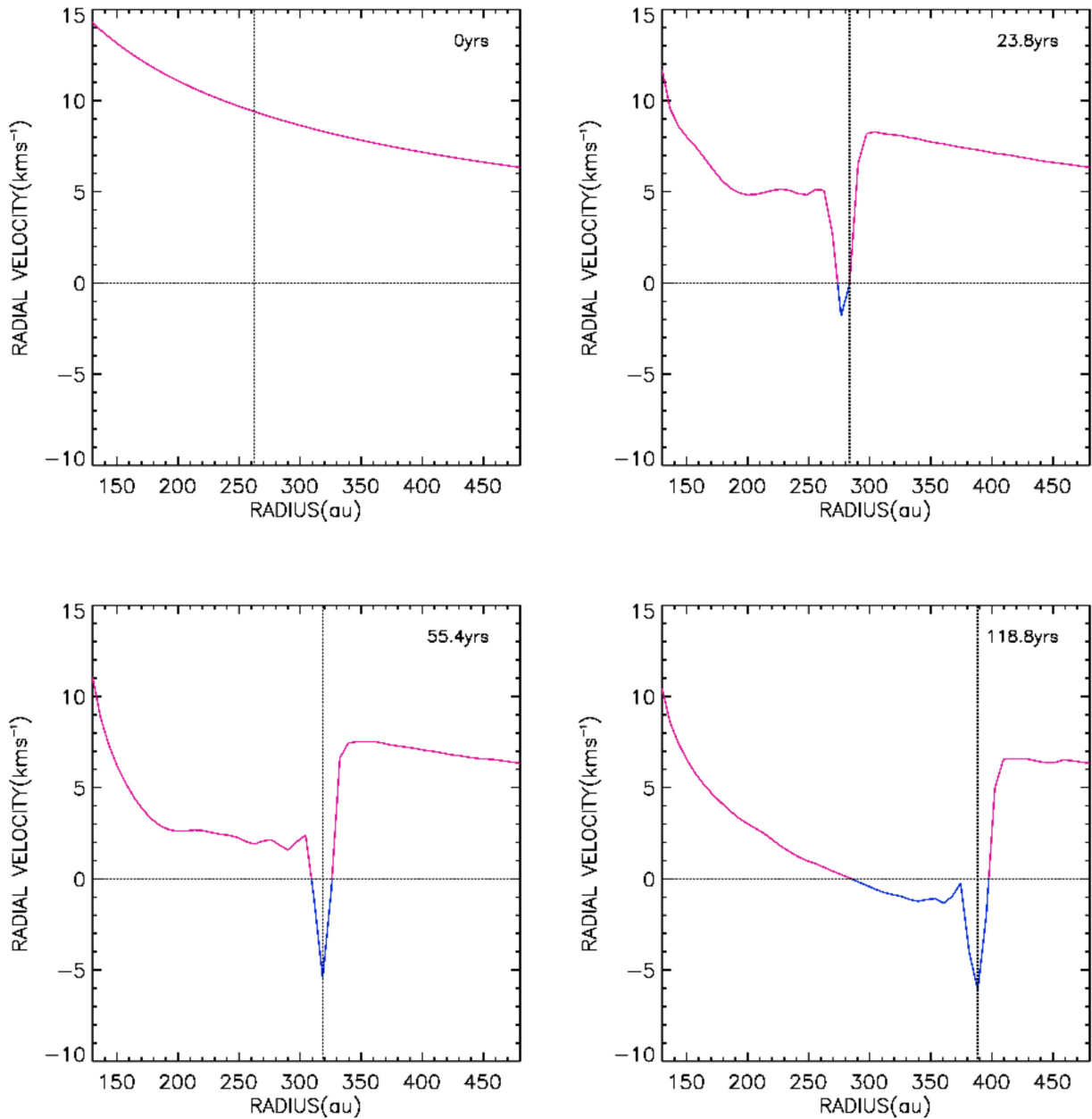


Figure 7. The radially averaged velocity profile at four different times during the late-time H II region expansion, a positive radial velocity corresponds to inward motion. Zero year marks the moment radiation is switched on. The simulation models a $17.87 M_{\odot}$ central star with a constant ionizing luminosity large enough for the ionization radius to exceed the ionized sonic point (~ 200 au). The vertical line represents the position of the ionization front. The horizontal line marks zero velocity, the point across which the velocity changes direction. The profile is pink where the velocity points towards the central star, and blue where the velocity points away from the star.

For velocities between v_R and v_D , there is no single front solution to the jump across the ionization boundary.

In order to investigate the evolution of the H II region past the R-critical radius, we repeated the simulation described in Section 3.2 for different luminosity values ionizing beyond this radius. The size of the simulation box was increased to $x, y, z \in [-480, 480]$ au, which in turn increased the inner and outer mask radii to 124.8 and 456.0 au. We found the H II region remains trapped and oscillating beyond the R-critical radius, until the ionized region extends beyond the ionized sonic point, at which point rapid expansion begins. The sonic point, where the infall velocity equals $c_i = 11.5 \text{ km s}^{-1}$, lies approximately at 200 au.

The results presented in Figs 6–8 are from a simulation using a luminosity of $Q = 2 \times 10^{46} \text{ s}^{-1}$, where the initial ionization radius reaches approximately 260 au, exceeding the sonic point and hence resulting in rapid expansion. The luminosity is smaller than that previously needed to ionize out to ~ 30 au because we are only ionizing material outside the inner mask, which in this simulation is further away from the star and thus at a much lower density.

The simulation shows an expanding ionization radius which is plotted as a function of time in Fig. 6. The discrete jump the ionization front makes every three to four time-steps is a result of the grid resolution. During the expansion phase, the neutral material is moving towards the central star due to gravity just as it would if

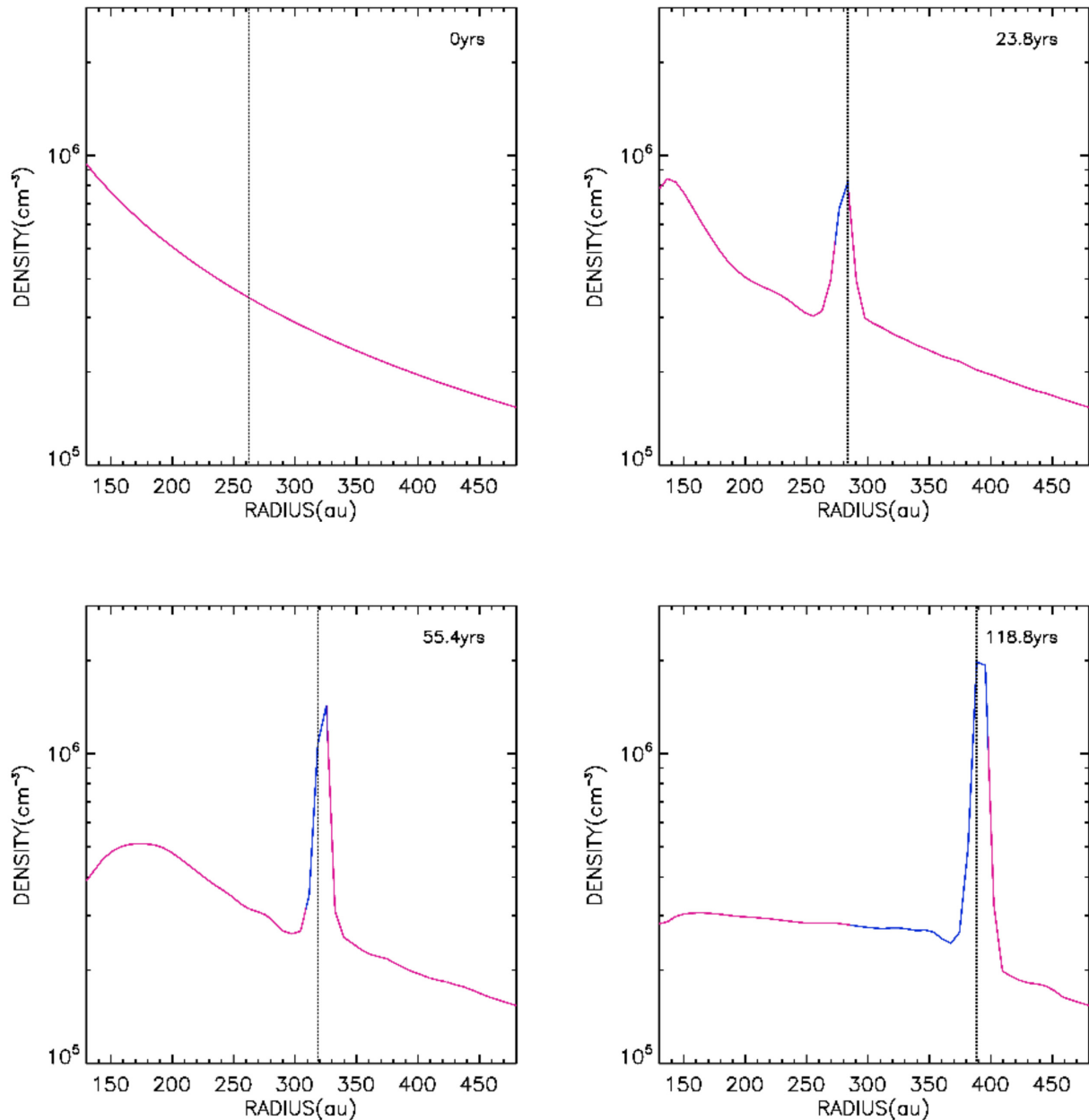


Figure 8. The radially averaged density profile at four different times during the late-time H II region expansion. Zero year marks the moment radiation is switched on. The simulation models a $17.87 M_{\odot}$ central star with a constant ionizing luminosity large enough for the ionization radius to exceed the ionized sonic point (~ 200 au). The vertical line represents the position of the ionization front. The profile is pink where the velocity points towards the central source, and blue where the velocity points away from the source. Note the decreasing density in the inner H II region where material is accreting and hence draining the H II region and shutting off accretion.

there was no radiation, until it reaches the expanding dense shell. The shell, along with most of the ionized material it accumulates, moves radially outwards, but close to the star ionized material still accretes. Figs 7 and 8 show the directions of motion of the material at four different time-steps, with red and blue indicating inflow and outflow, respectively. The material inside the H II region is not replenished, since no material crosses the ionization front, meaning the region is eventually drained.

The transition point from trapped to expanding can be used to estimate the time-scale of the UCH II region phase. The Wood &

Churchwell (1989) survey indicates 10 per cent of all O and B stars are surrounded by a UCH II region. This suggests the lifetime of UCH II regions must exceed 10^5 yr, which is longer than the time it would take an UCH II region to evolve to a diffuse H II region through pressure-driven expansion (Wood & Churchwell 1989). During the time it takes to accrete enough material on to our central star to reach a high enough mass corresponding to a high enough luminosity to ionize past the sonic point, the H II region will remain trapped. Including this period before the expansion phase begins increases the total lifetime of UCH II regions.

4 CONCLUSIONS

We have presented the first look at the steady-state models of H II region evolution within spherically symmetric Bondi accretion flows by Keto (2002b, 2003) and Mestel (1954) in a radiation hydrodynamic framework. Our numerical radiation hydrodynamic simulations reproduce the main features of the analytic steady-state analyses, namely gravitationally trapped H II regions at early times and pressure-driven expansion when the ionizing luminosity increases to produce an H II region extending beyond the critical radius at approximately the ionized sonic point.

The main difference between the analytical work and our simulations is the stability of the trapped H II region. Any increase in density within the ionized region, whether due to jump conditions across the ionization front or noise in the simulation, initiates a runaway instability of the H II region. This instability is expected to occur only in idealized spherically symmetric geometry.

Regardless of the H II region oscillation, our results are in broad agreement with the analyses by Keto (2002b, 2003) and Mestel (1954). The implication of this picture on massive star formation is that accretion of material on to forming stars can continue even after the star starts emitting ionizing radiation (see also Kuiper & Hosokawa 2018). This is because the H II region remains gravitationally trapped, and all velocities are inflowing, until the ionizing luminosity grows (due to mass accretion) and the radius of ionization passes the critical radius where pressure-driven expansion begins. At this stage, the accretion rate on to the star decreases to zero and the star reaches its maximum accreted mass. This could change estimates of the accretion rate during the UCH II phase of formation of high-mass stars as the accretion period can last for longer. Furthermore, gravitational trapping could also help explain the surprisingly long lifetimes of UCH II regions.

The next paper in this series will investigate the discovered instability analytically as well as with a 1D code capable of much higher resolution than our idealized 3D simulations. The simulations presented in this paper produce spherically symmetric ionized accretion flows in an isolated system; no rotation or magnetic fields are introduced. This simplified approach is necessary for a direct comparison to the analytical model presented by Keto (2002b, 2003) and Mestel (1954); however, it is not a realistic treatment of the evolution of H II regions. Future work will explore radiation hydrodynamic simulations of rotationally flattened ionized accretion structures comprising equatorial inflow and simultaneous bipolar outflows (Keto 2007) and the production of synthetic continuum and line intensity maps to compare with observations.

ACKNOWLEDGEMENTS

We thank the anonymous referee for helpful comments. KL acknowledges financial support from the Carnegie Trust. KW, DFG, and BV acknowledge support from STFC grant ST/M001296/1.

DFG thanks the Brazilian agencies CNPq (no. 311128/2017-3) and FAPESP (no. 2013/10559-5) for financial support. NS thanks CAPES for the financial support.

REFERENCES

- Bisbas T. G. et al., 2015, *MNRAS*, 453, 1324
 Bondi H., 1952, *MNRAS*, 112, 195
 Falceta-Gonçalves D., Kowal G., 2015, *ApJ*, 808, 65
 Falceta-Gonçalves D., Bonnell I., Kowal G., Lépine J. R. D., Braga C. A. S., 2015, *MNRAS*, 446, 973
 Harries T. J., Douglas T. A., Ali A., 2017, *MNRAS*, 471, 4111
 Haworth T. J., Harries T. J., 2012, *MNRAS*, 420, 562
 He Z., Li X., Fu D., Ma Y., 2011, *Sci. China Phys. Mech. Astron.*, 54, 511
 Keto E., 2002a, *ApJ*, 568, 754
 Keto E., 2002b, *ApJ*, 580, 980
 Keto E., 2003, *ApJ*, 599, 1196
 Keto E., 2007, *ApJ*, 666, 976
 Keto E., Wood K., 2006, *ApJ*, 637, 850
 Klaassen P. D. et al., 2018, *A&A*, 611, A99
 Klaassen P. D., Wilson C. D., 2007, *ApJ*, 663, 1092
 Kowal G., Falceta-Gonçalves D. A., Lazarian A., 2011, *New J. Phys.*, 13, 053001
 Kowal G., Falceta-Gonçalves D. A., Lazarian A., Vishniac E. T., 2017, *ApJ*, 838, 91
 Krumholz M. R., Klein R. I., McKee C. F., Offner S. S. R., Cunningham A. J., 2009, *Science*, 323, 754
 Kuiper R., Hosokawa T., 2018, *A&A*, 616, A101
 Kuiper R., Klahr H., Beuther H., Henning T., 2010, *ApJ*, 722, 1556
 Lucy L. B., 1999, *A&A*, 344, 282
 Mestel L., 1954, *MNRAS*, 114, 437
 Mignone A., Bodo G., 2006, *MNRAS*, 368, 1040
 Nakano T., 1989, *ApJ*, 345, 464
 Osterbrock D. E., Ferland G. J., 2006, *Astrophysics of Gaseous Nebulae and Active Galactic Nuclei*, University Science Books, Sausalito, California
 Peters T., Banerjee R., Klessen R. S., Mac Low M.-M., Galván-Madrid R., Keto E. R., 2010, *ApJ*, 711, 1017
 Ruuth S. J., 2006, *Math. Comput.*, 75, 183
 Santos-Lima R., de Gouveia Dal Pino E. M., Falceta-Gonçalves D. A., Nakwacki M. S., Kowal G., 2017, *MNRAS*, 465, 4866
 Sollins P. K., Zhang Q., Keto E., Ho P. T. P., 2005a, *ApJ*, 624, L49
 Sollins P. K., Zhang Q., Keto E., Ho P. T. P., 2005b, *ApJ*, 631, 399
 Spitzer L., 1978, *Physical Processes in the Interstellar Medium*, John Wiley & Sons, New York
 Vacca W. D., Garmany C. D., Shull J. M., 1996, *ApJ*, 460, 914
 Vandenbroucke B., et al., 2019, *MNRAS*, 485, 3771
 Wood K., Loeb A., 2000, *ApJ*, 545, 86
 Wood K., Reynolds R. J., 1999, *ApJ*, 525, 799
 Wood K., Mathis J. S., Ercolano B., 2004, *MNRAS*, 348, 1337
 Wood D. O. S., Churchwell E., 1989, *ApJS*, 69, 831
 Yorke H. W., Sonnhalter C., 2002, *ApJ*, 569, 846

This paper has been typeset from a $\text{\TeX}/\text{\LaTeX}$ file prepared by the author.